# Supplementary Information: Quantum spin liquid and Mott insulator phases in the $Mo_3O_8$ cluster systems

S. A. Nikolaev,[1,2,*] I. V. Solovyev,[2,3] and S. V. Streltsov[4,3]

[1] *Institute of Innovative Research, Tokyo Institute of Technology, 4259 Nagatsuta, Midori, Yokohama 226-8503, Japan*
[2] *International Center for Materials Nanoarchitectonics, National Institute for Materials Science, 1-1 Namiki, Tsukuba, Ibaraki 305-0044, Japan*
[3] *Department of Theoretical Physics and Applied Mathematics, Ural Federal University, Mira St. 19, 620002 Yekaterinburg, Russia*
[4] *Institute of Metal Physics, S. Kovalevskoy Street 18, 620108 Yekaterinburg, Russia*

## SUPPLEMENTARY NOTE 1: ONE-ORBITAL EXTENDED HUBBARD MODEL

A single-orbital extended Hubbard model on the anisotropic kagomé lattice formed by the down-oriented $\mathcal{T}$ and up-oriented $\mathcal{T}'$ triangles is defined as:

$$\begin{aligned}\mathcal{H} = \mathcal{H}_{\rm kin} + \mathcal{H}_{\rm int} = &\sum_{\substack{\langle mm'\rangle\in\mathcal{T}\\ \sigma}} \left(tc_m^{\dagger\sigma}c_{m'}^{\sigma} + tc_{m'}^{\dagger\sigma}c_m^{\sigma} + Vn_m^{\sigma}n_{m'}^{\bar\sigma} + (V-J)n_m^{\sigma}n_{m'}^{\sigma}\right)\\ &+ \sum_{\substack{\langle mm'\rangle\in\mathcal{T}'\\ \sigma'}} \left(t'c_m^{\dagger\sigma}c_{m'}^{\sigma} + t'c_{m'}^{\dagger\sigma}c_m^{\sigma} + V'n_m^{\sigma}n_{m'}^{\bar\sigma} + (V'-J')n_m^{\sigma}n_{m'}^{\sigma}\right) + U\sum_m n_m^{\uparrow}n_m^{\downarrow},\end{aligned} \tag{1}$$

where $c_m^{\dagger\sigma}$ ($c_m^{\sigma}$) creates (annihilates) an electron with spin $\sigma$ at site $m$, $t$ and $t'$ stand for intracluster and intercluster hopping parameters along the $\mathcal{T}$ and $\mathcal{T}'$, respectively. The interaction term $\mathcal{H}_{\rm int}$ includes the on-site $U$, intracluster $V$, and intercluster $V'$ Coulomb interactions, as well as the intracluster $J$ and intercluster $J'$ exchange interactions, defined in the basis of Wannier functions $w(\mathbf{r})$:

$$\begin{aligned}U &= \int d\mathbf{r}d\mathbf{r}' w_m^{\dagger}(\mathbf{r})w_m(\mathbf{r})U(\mathbf{r},\mathbf{r}')w_m^{\dagger}(\mathbf{r}')w_m(\mathbf{r}'),\\ V &= \int d\mathbf{r}d\mathbf{r}' w_m^{\dagger}(\mathbf{r})w_m(\mathbf{r})U(\mathbf{r},\mathbf{r}')w_{m'}^{\dagger}(\mathbf{r}')w_{m'}(\mathbf{r}') \qquad \text{for } \langle mm'\rangle\in\mathcal{T},\\ J &= \int d\mathbf{r}d\mathbf{r}' w_m^{\dagger}(\mathbf{r})w_{m'}(\mathbf{r})U(\mathbf{r},\mathbf{r}')w_{m'}^{\dagger}(\mathbf{r}')w_m(\mathbf{r}') \qquad \text{for } \langle mm'\rangle\in\mathcal{T},\\ V' &= \int d\mathbf{r}d\mathbf{r}' w_m^{\dagger}(\mathbf{r})w_m(\mathbf{r})U(\mathbf{r},\mathbf{r}')w_{m'}^{\dagger}(\mathbf{r}')w_{m'}(\mathbf{r}') \qquad \text{for } \langle mm'\rangle\in\mathcal{T}',\\ J' &= \int d\mathbf{r}d\mathbf{r}' w_m^{\dagger}(\mathbf{r})w_{m'}(\mathbf{r})U(\mathbf{r},\mathbf{r}')w_{m'}^{\dagger}(\mathbf{r}')w_m(\mathbf{r}') \qquad \text{for } \langle mm'\rangle\in\mathcal{T}',\end{aligned} \tag{2}$$

where $U(\mathbf{r},\mathbf{r}')$ is the partially screened Coulomb interaction. On account of its small contribution, we have neglected a "pair-hopping"-like term, $\sim w_m^{\dagger}(\mathbf{r})w_{m'}(\mathbf{r})U(\mathbf{r},\mathbf{r}')w_m^{\dagger}(\mathbf{r}')w_{m'}(\mathbf{r}')$. We consider the case of 1/6 filling and assume that the on-site $U > V \sim V'$ is the largest parameter.

## SUPPLEMENTARY NOTE 2: QUANTUM DIMER MODEL

Assuming that $U > V \sim V' \gg |t| \sim |t'|$, the on-site Coulomb interaction $U$ can be discarded, because all double occupied states at 1/6 filling lie higher in energy. In the absence of electron hoppings, the intersite Coulomb interactions are minimised when each corner-sharing triangle hosts exactly one electron, and as a result the system displays a highly degenerate ground state of all possible patterns with the singly occupied $\mathcal{T}$ and $\mathcal{T}'$ triangles, as shown in Supplementary Figure 1a. This degeneracy can further be lifted upon including hopping processes that give rise to the collective motion of electrons, so that they hop clockwise and counter-clockwise around the hexagons either along $\mathcal{T}$ or along $\mathcal{T}'$, as shown in Supplementary Figure 1b. As a result, the charge order III from Supplementary Figure 1a covered by two elementary plaquette states with three electrons at the hexagons, $|\mathbb{A}\rangle = c_5^{\dagger\sigma}c_3^{\dagger\sigma'}c_1^{\dagger\sigma''}|0\rangle$ and $|\mathbb{B}\rangle = c_6^{\dagger\sigma}c_4^{\dagger\sigma'}c_2^{\dagger\sigma''}|0\rangle$, is stabilised. The corresponding energy gain is obtained in a perturbative expansion with respect to $\mathcal{H}_{\rm kin}$ to third order in $t/V'$ and $t'/V$:

$$E_{\rm n}^{(3)} = \sum_{k\neq n}\sum_{m\neq n}\frac{\langle n|\mathcal{H}_{\rm kin}|m\rangle\langle m|\mathcal{H}_{\rm kin}|k\rangle\langle k|\mathcal{H}_{\rm kin}|n\rangle}{\left(E_n^{(0)}-E_m^{(0)}\right)\left(E_n^{(0)}-E_k^{(0)}\right)}, \tag{3}$$

where $E_{\rm n}^{(0)}$ is the interaction energy of an electronic configuration $|n\rangle$ given by $\mathcal{H}_{\rm int}$, that yields:

$$\begin{aligned}\mathcal{H}^{(3)} = &\frac{6t^3}{V'^2}\left(c_5^{\dagger\sigma}c_4^{\sigma}c_3^{\dagger\sigma'}c_2^{\sigma'}c_1^{\dagger\sigma''}c_6^{\sigma''} + c_2^{\dagger\sigma}c_3^{\sigma}c_4^{\dagger\sigma'}c_5^{\sigma'}c_6^{\dagger\sigma''}c_1^{\sigma''}\right)\\ &+ \frac{6t'^3}{V^2}\left(c_3^{\dagger\sigma}c_4^{\sigma}c_5^{\dagger\sigma'}c_6^{\sigma'}c_1^{\dagger\sigma''}c_2^{\sigma''} + c_6^{\dagger\sigma}c_5^{\sigma}c_4^{\dagger\sigma'}c_3^{\sigma'}c_2^{\dagger\sigma''}c_1^{\sigma''}\right).\end{aligned} \tag{4}$$

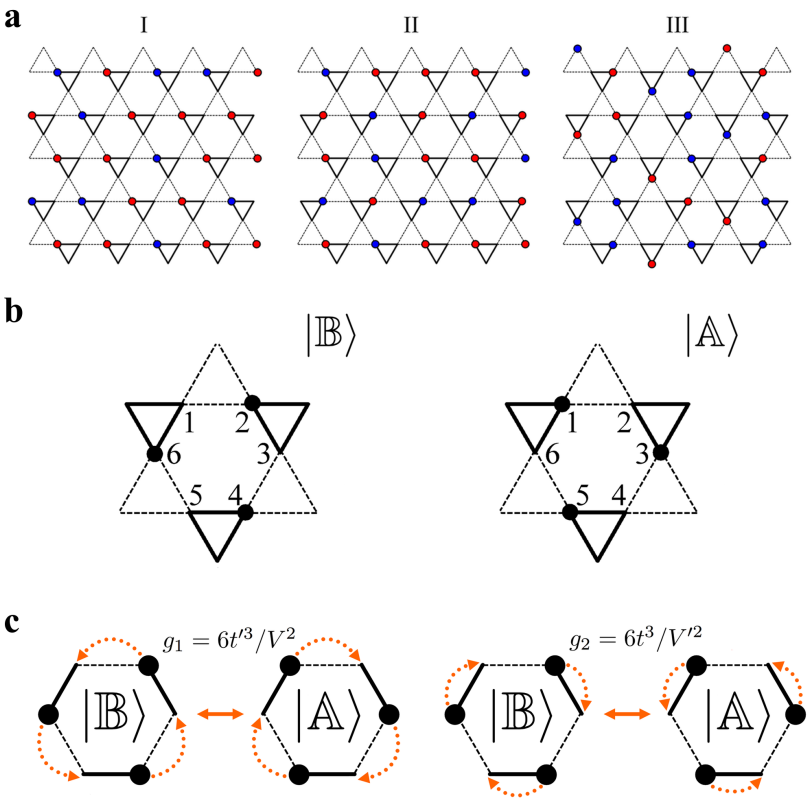


**Supplementary Figure 1**. **a** Possible charge ordering patterns on the 1/6-filled kagomé lattice (blue and red circles stand for the spin-up and spin-down electrons, respectively). **b** Elementary plaquettes of the quantum dimer model. **c** Ring tunnelling processes connecting elementary plaquettes at each hexagon.

Summing up over all hexagons and spin configurations and replacing $c_1^{\dagger\sigma}c_2^{\sigma}c_3^{\dagger\sigma'}c_4^{\sigma'}c_5^{\dagger\sigma''}c_6^{\sigma''} = c_5^{\dagger\sigma''}c_3^{\dagger\sigma'}c_1^{\dagger\sigma}c_2^{\sigma}c_4^{\sigma'}c_6^{\sigma''} = |\mathbb{A}\rangle\langle\mathbb{B}|$, we obtain:

$$\mathcal{H}_{\hexagon} = \sum_{\hexagon} \sum_{\sigma\sigma'\sigma''} (g_1 + g_2) h_{\hexagon}, \qquad h_{\hexagon} = |\mathbb{A}\rangle\langle\mathbb{B}| + |\mathbb{B}\rangle\langle\mathbb{A}| \tag{5}$$

with $g_1 = 6t'^3/V^2$ and $g_2 = 6t^3/V'^2$. The resulting low-energy model has the form of the quantum dimer model for the hard-core plaquette states $|\mathbb{A}\rangle$ and $|\mathbb{B}\rangle$:

$$\mathcal{H}_{\mathrm{DM}} = -t_{\mathrm{D}} \sum_{\hexagon} \big(|\mathbb{A}\rangle\langle\mathbb{B}| + |\mathbb{B}\rangle\langle\mathbb{A}|\big) + v_{\mathrm{D}} \sum_{\hexagon} \big(|\mathbb{A}\rangle\langle\mathbb{A}| + |\mathbb{B}\rangle\langle\mathbb{B}|\big), \tag{6}$$

where the first term $\sim t_{\mathrm{D}}$ is a kinetic term that flips hexagonal plaquettes, and the second term $\sim v_{\mathrm{D}}$ is a potential that counts the number of flippable plaquettes, i.e. $v_{\mathrm{D}} < 0$ ($> 0$) favours (disfavours) such plaquettes. The phase diagram of this model for spinless electrons is shown in Supplementary Figure 2 [1, 2], featuring three distinct phases that belong to two different topological sectors which are not flip connected: on the one hand, the so-called star charge ordered ($-0.228 < v_{\mathrm{D}}/t_{\mathrm{D}} < 1$) and plaquette charge ordered states ($v_{\mathrm{D}}/t_{\mathrm{D}} < -0.228$), and on the other hand a staggered charge ordered state ($v_{\mathrm{D}}/t_{\mathrm{D}} > 1$), in which all hexagon plaquettes are destroyed. Given that $v_{\mathrm{D}} = 0$ in Eq. (5), the ground state of Eq. (1) in the limit $|t|/V' \ll 1$ and $|t'|/V \ll 1$ is expected to reveal a plaquette charge order with resonating hexagons.

The quantum dimer model for spinful electrons can also include antiferromagnetic spin fluctuations between next-nearest neighbours $\langle\langle ij \rangle\rangle$ at each hexagon (for example, 1–3, 3–5, and 5–1 in $|\mathbb{A}\rangle$), which are obtained to second order in $t_{\mathrm{nn}}/U$:

$$E_{\mathrm{n}}^{(2)} = \sum_{m \neq n} \frac{\langle n|\mathcal{H}_{\mathrm{kin}}|m\rangle\langle m|\mathcal{H}_{\mathrm{kin}}|n\rangle}{\big(E_n^{(0)} - E_m^{(0)}\big)}, \tag{7}$$

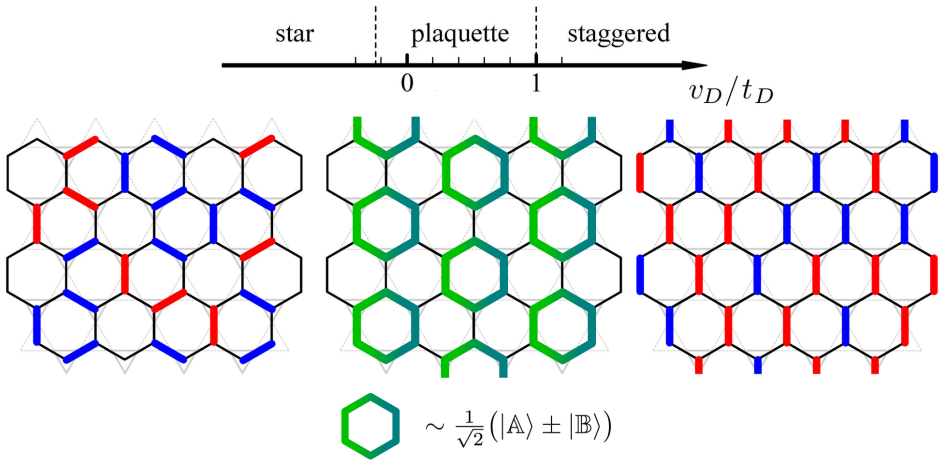


**Supplementary Figure 2**. Phase diagram of the quantum dimer model for spinless electrons on the dual hexagonal lattice [1, 2]. Blue and red links encode the spin-up and spin-down electrons, respectively, and the green colour corresponds to the resonating hexagons.

that gives

$$\mathcal{H}_{\rm S} = J_{\rm nn} \sum_{\langle\langle ij \rangle\rangle} n_i n_j \big(\mathbf{S}_i \cdot \mathbf{S}_j - \frac{1}{4}\big) \tag{8}$$

with $J_{\rm nn} = 4t_{\rm nn}^2/U$, where $t_{\rm nn}$ is the hopping parameter between next-nearest neighbours; $n_i$ is the occupation number at site $i$, and $n_i n_j$ emphasises that $J_{\rm nn}$ couples only occupied sites because the electron positions are not fixed in the hexagon.

The final form of the low-energy model reads:

$$\mathcal{H}_{\rm D} = \mathcal{H}_{\hexagon} + \mathcal{H}_{\rm S}. \tag{9}$$

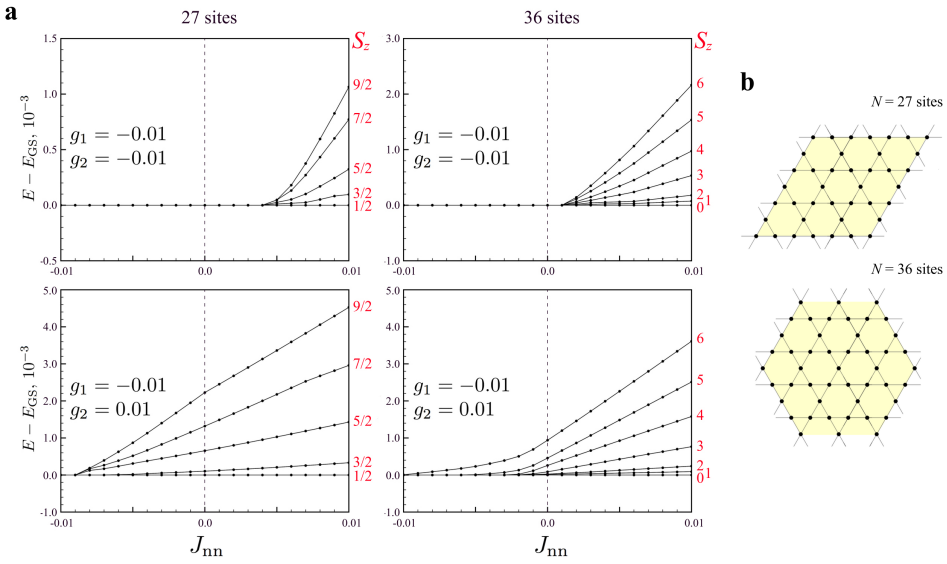


**Supplementary Figure 3**. **a** Ground state energies per site for different $S_z$ sectors of the quantum dimer model, Eq. (9), as obtained from exact diagonalisation for finite geometries with periodic boundary conditions containing $N = 27$ and 36 sites. The difference with the lowest energy level $E_{\rm GS}$ is shown. **b** Geometries used for exact diagonalisation with $N = 27$ and 36 sites

The results of exact diagonalisation for the quantum dimer model (9) are presented in Supplementary Figure 3. One can see that when $g_1$ and $g_2$ have the same sign the ground state is highly degenerate, and the different spin sectors with total spin $S_z$ can further be split by exchange interactions $J_{\rm nn}$ between next-nearest neighbours, in agreement with Ref. [3]. However, when $g_1$ and $g_2$ have opposite signs the degeneracy of the different spin sectors is lifted even in the absence of spin fluctuations, which is at variance with Ref. [3]. When $g_1$ and $g_2$ have the same sign, the matrix elements of $\mathcal{H}_{\hexagon}$ can be chosen positive owing to the bipartite lattice, and the Perron-Frobenius theorem can be applied to show the degeneracy of different spin sectors, as was done in Ref. [3]. This is no longer true in the case of opposite signs, when $\mathcal{H}_{\hexagon}$ contains both positive and negative entries and the theorem is not applicable.

Density-density, spin-spin, and plaquette-plaquette correlation functions are used to characterise the PCO state:

$$C^{\rm n}(\mathbf{r}_0,\mathbf{r}_k)=\langle n(\mathbf{r}_0)n(\mathbf{r}_k)\rangle-\langle n(\mathbf{r}_0)\rangle\langle n(\mathbf{r}_k)\rangle, \tag{10}$$

$$C^{\rm s}(\mathbf{r}_0,\mathbf{r}_k)=\langle \mathbf{S}(\mathbf{r}_0)\cdot\mathbf{S}(\mathbf{r}_k)\rangle-\langle \mathbf{S}(\mathbf{r}_0)\rangle\cdot\langle \mathbf{S}(\mathbf{r}_k)\rangle, \tag{11}$$

$$C^{\rm h}(\mathbf{R}_0,\mathbf{R}_k)=\langle h_{\hexagon}(\mathbf{R}_0)h_{\hexagon}(\mathbf{R}_k)\rangle-\langle h_{\hexagon}(\mathbf{R}_0)\rangle\langle h_{\hexagon}(\mathbf{R}_k)\rangle, \tag{12}$$

respectively, and the corresponding static structure factors are calculated as (for $i=$ n, s, and h):

$$S^i(\mathbf{q})=\frac{1}{N}\sum_k e^{-i\mathbf{q}\cdot(\mathbf{r}_k-\mathbf{r}_0)}C^i(\mathbf{r}_0,\mathbf{r}_k). \tag{13}$$

The resulting correlation functions for $\mathcal{H}_{\hexagon}$ and $\mathcal{H}_{\rm S}$ obtained from exact diagonalisation are shown in Supplementary Figure 4. The calculated $C^{\rm h}$ clearly demonstrates the formation of resonating hexagons in $\mathcal{H}_{\hexagon}$, and the corresponding $C^{\rm n}$ and $C^{\rm s}$ show short-range correlations in $\mathcal{H}_{\hexagon}$ melting down with distance. These results are in agreement with Ref. [4].

In the plaquette charge ordered state, the resonating hexagons can be effectively decoupled, so that one can consider a single hexagon containing three electrons in the basis of plaquette states $|\sigma_1\sigma_2\sigma_3\rangle_{\mathbb{A}}\oplus|\sigma_1\sigma_2\sigma_3\rangle_{\mathbb{B}}$, where the Hilbert space at each plaquette spans all possible spin configurations $|\sigma_1\sigma_2\sigma_3\rangle=\{|\uparrow\uparrow\uparrow\rangle,|\uparrow\uparrow\downarrow\rangle,|\uparrow\downarrow\uparrow\rangle,|\uparrow\downarrow\downarrow\rangle,|\downarrow\uparrow\uparrow\rangle,|\downarrow\uparrow\downarrow\rangle,|\downarrow\downarrow\uparrow\rangle,|\downarrow\downarrow\downarrow\rangle\}$. The isotropic exchange within each plaquette is written as:

$$\mathcal{H}_{\rm S}=\begin{pmatrix}
\frac{3J_{\rm nn}}{4} & 0 & 0 & 0 & 0 & 0 & 0 & 0\\
0 & -\frac{J_{\rm nn}}{4} & \frac{J_{\rm nn}}{2} & 0 & \frac{J_{\rm nn}}{2} & 0 & 0 & 0\\
0 & \frac{J_{\rm nn}}{2} & -\frac{J_{\rm nn}}{4} & 0 & \frac{J_{\rm nn}}{2} & 0 & 0 & 0\\
0 & 0 & 0 & -\frac{J_{\rm nn}}{4} & 0 & \frac{J_{\rm nn}}{2} & \frac{J_{\rm nn}}{2} & 0\\
0 & \frac{J_{\rm nn}}{2} & \frac{J_{\rm nn}}{2} & 0 & -\frac{J_{\rm nn}}{4} & 0 & 0 & 0\\
0 & 0 & 0 & \frac{J_{\rm nn}}{2} & 0 & -\frac{J_{\rm nn}}{4} & \frac{J_{\rm nn}}{2} & 0\\
0 & 0 & 0 & \frac{J_{\rm nn}}{2} & 0 & \frac{J_{\rm nn}}{2} & -\frac{J_{\rm nn}}{4} & 0\\
0 & 0 & 0 & 0 & 0 & 0 & 0 & \frac{3J_{\rm nn}}{4}
\end{pmatrix}, \tag{14}$$

and gives two four-fold degenerate states satisfying $\frac{1}{2}\otimes\frac{1}{2}\otimes\frac{1}{2}=\frac{1}{2}\oplus\frac{1}{2}\oplus\frac{3}{2}$:

$$\begin{aligned}
E^{(\rm S1)}&=\frac{3J_{\rm nn}}{4} & |\psi_1^{(\rm S1)}\rangle&=|\uparrow\uparrow\uparrow\rangle,\\
& & |\psi_2^{(\rm S1)}\rangle&=\tfrac{1}{\sqrt{3}}(|\uparrow\uparrow\downarrow\rangle+|\uparrow\downarrow\uparrow\rangle+|\downarrow\uparrow\uparrow\rangle),\\
& & |\psi_3^{(\rm S1)}\rangle&=\tfrac{1}{\sqrt{3}}(|\uparrow\downarrow\downarrow\rangle+|\downarrow\uparrow\downarrow\rangle+|\downarrow\downarrow\uparrow\rangle),\\
& & |\psi_4^{(\rm S1)}\rangle&=|\downarrow\downarrow\downarrow\rangle,\\
E^{(\rm S2)}&=-\frac{3J_{\rm nn}}{4} & |\psi_1^{(\rm S2)}\rangle&=\tfrac{1}{\sqrt{2}}(|\uparrow\uparrow\downarrow\rangle-|\downarrow\uparrow\uparrow\rangle),\\
& & |\psi_2^{(\rm S2)}\rangle&=\tfrac{1}{\sqrt{2}}(|\uparrow\downarrow\uparrow\rangle-|\downarrow\uparrow\uparrow\rangle),\\
& & |\psi_3^{(\rm S2)}\rangle&=\tfrac{1}{\sqrt{2}}(|\uparrow\downarrow\downarrow\rangle-|\downarrow\downarrow\uparrow\rangle),\\
& & |\psi_4^{(\rm S2)}\rangle&=\tfrac{1}{\sqrt{2}}(|\downarrow\uparrow\downarrow\rangle-|\downarrow\downarrow\uparrow\rangle).
\end{aligned} \tag{15}$$

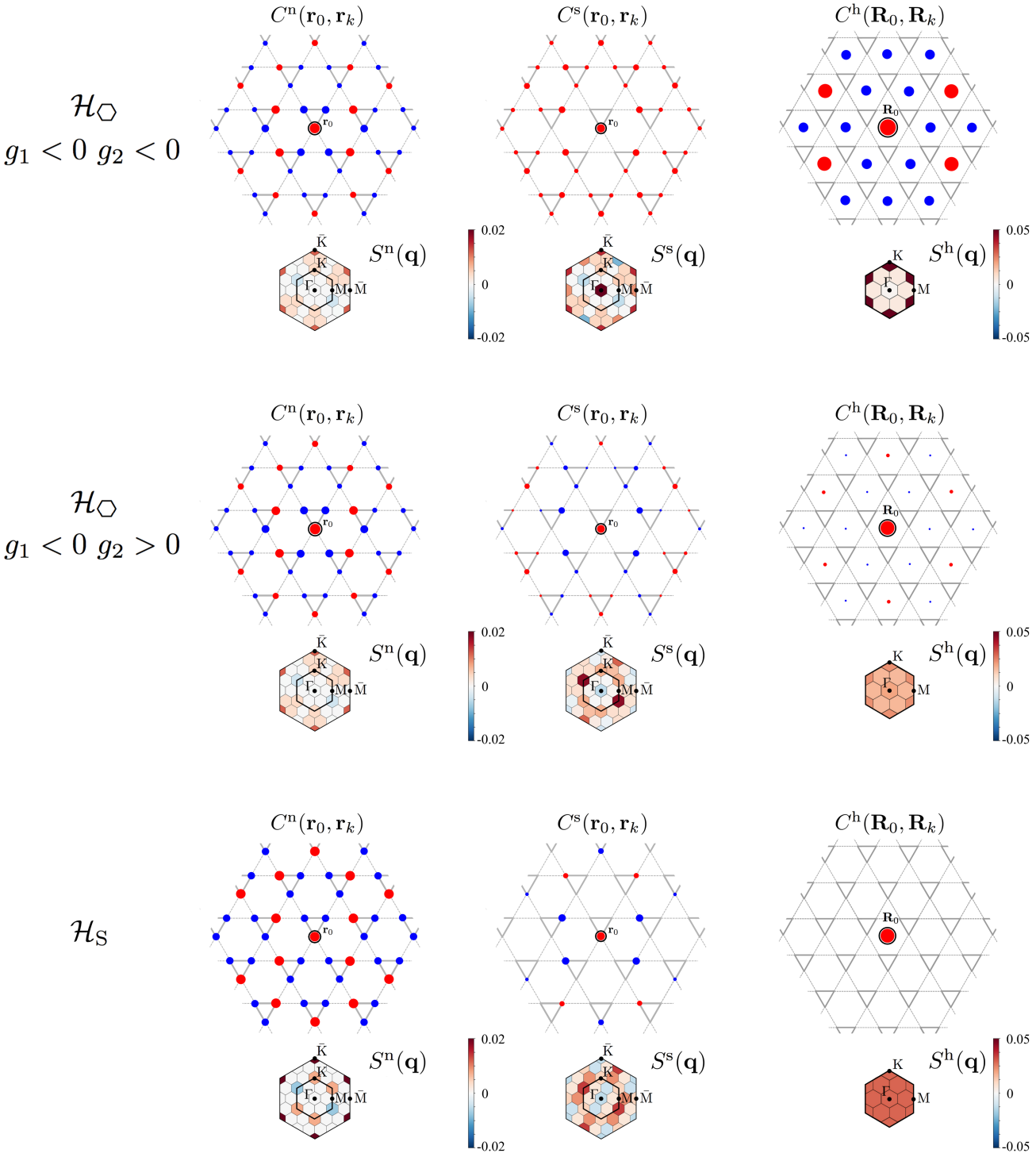


**Supplementary Figure 4**. Density-density $C^{\mathrm{n}}(\mathbf{r}_0, \mathbf{r}_k)$, spin-spin $C^{\mathrm{s}}(\mathbf{r}_0, \mathbf{r}_k)$, and plaquette-plaquette $C^{\mathrm{h}}(\mathbf{R}_0, \mathbf{R}_k)$ correlation functions and the corresponding static structure factors, $S^{\mathrm{n}}(\mathbf{q})$, $S^{\mathrm{s}}(\mathbf{q})$, and $S^{\mathrm{h}}(\mathbf{q})$, of the quantum dimer models: $\mathcal{H}_{\hexagon}$ with $g_1 = -0.01$, $g_2 = -0.01$, $\mathcal{H}_{\hexagon}$ with $g_1 = -0.02$, $g_2 = 0.01$, and $\mathcal{H}_{\mathrm{S}}$ with $J_{\mathrm{nn}} = 0.01$, as obtained from exact diagonalisation for finite geometries containing $N = 27$ and 36 sites with periodic boundary conditions. The radius of the dots is proportional to the absolute value of the correlation function, and the colour encodes the sign (red for a positive value, blue for a negative value). Here, $S^{\mathrm{h}}(\mathbf{q})$ is calculated on the original Brillouin zone; $S^{\mathrm{n}}(\mathbf{q})$ and $S^{\mathrm{s}}(\mathbf{q})$ are calculated on the extended Brillouin zone (double of the original one).

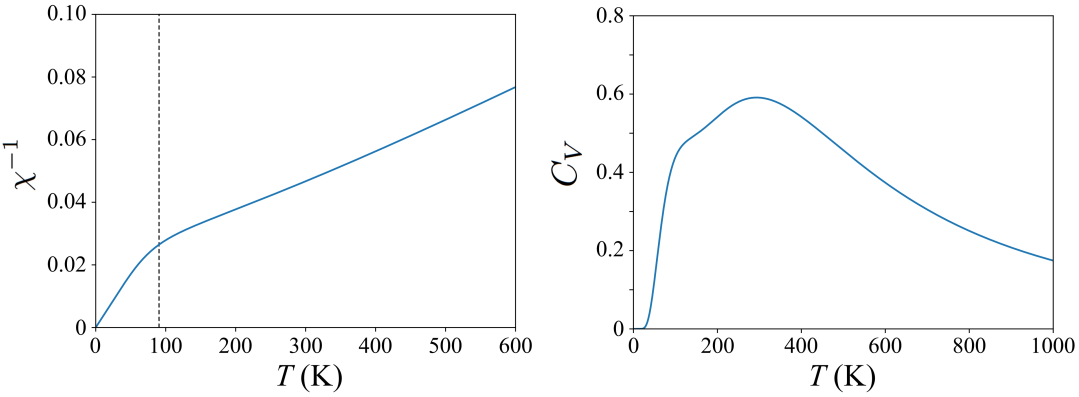


**Supplementary Figure 5**. Specific heat and spin susceptibility of a single hexagon calculated with the model parameters for $LiZn_2Mo_3O_8$: $g_1 = 13.5$ meV, $g_2 = -40.1$ meV, and $J_{\rm nn} = 1.4$ meV.

In turn, the ring tunnelling processes are given as:

$$\mathcal{H}_{\mathbb{A}\to\mathbb{B}} = \mathcal{H}^{\rm T}_{\mathbb{B}\to\mathbb{A}} = \begin{pmatrix} g_1+g_2 & 0 & 0 & 0 & 0 & 0 & 0 & 0 \\ 0 & g_1 & g_2 & 0 & 0 & 0 & 0 & 0 \\ 0 & 0 & g_1 & 0 & g_2 & 0 & 0 & 0 \\ 0 & 0 & 0 & g_1 & 0 & 0 & g_2 & 0 \\ 0 & g_2 & 0 & 0 & g_1 & 0 & 0 & 0 \\ 0 & 0 & 0 & g_2 & 0 & g_1 & 0 & 0 \\ 0 & 0 & 0 & 0 & 0 & g_2 & g_1 & 0 \\ 0 & 0 & 0 & 0 & 0 & 0 & 0 & g_1+g_2 \end{pmatrix}. \tag{16}$$

The full Hamiltonian for a single hexagon has the following form:

$$\mathcal{H}_{\rm D} = \left(\begin{array}{c|c} \mathcal{H}_{\rm S} & \mathcal{H}_{\mathbb{A}\to\mathbb{B}} \\ \hline \mathcal{H}_{\mathbb{B}\to\mathbb{A}} & \mathcal{H}_{\rm S} \end{array}\right), \tag{17}$$

that yields four fourfold degenerate states:

$$E^{(\rm D1)} = -\frac{3}{4}J_{\rm nn} - \sqrt{g_1^2 - g_1g_2 + g_2^2}$$

$$\begin{aligned}
|\psi_1^{(\rm D1)}\rangle &= \tfrac{1}{2}\Big(|{\uparrow\uparrow\downarrow}\rangle_{\mathbb{A}} - |{\downarrow\uparrow\uparrow}\rangle_{\mathbb{A}} - \tfrac{g_1-g_2}{\tilde{g}}|{\uparrow\uparrow\downarrow}\rangle_{\mathbb{B}} - \tfrac{g_2}{\tilde{g}}|{\uparrow\downarrow\uparrow}\rangle_{\mathbb{B}} + \tfrac{g_1}{\tilde{g}}|{\downarrow\uparrow\uparrow}\rangle_{\mathbb{B}}\Big), \\
|\psi_2^{(\rm D1)}\rangle &= \tfrac{1}{2}\Big(|{\uparrow\downarrow\uparrow}\rangle_{\mathbb{A}} - |{\downarrow\uparrow\uparrow}\rangle_{\mathbb{A}} + \tfrac{g_2}{\tilde{g}}|{\uparrow\uparrow\downarrow}\rangle_{\mathbb{B}} - \tfrac{g_1}{\tilde{g}}|{\uparrow\downarrow\uparrow}\rangle_{\mathbb{B}} + \tfrac{g_1-g_2}{\tilde{g}}|{\downarrow\uparrow\uparrow}\rangle_{\mathbb{B}}\Big), \\
|\psi_3^{(\rm D1)}\rangle &= \tfrac{1}{2}\Big(|{\uparrow\downarrow\downarrow}\rangle_{\mathbb{A}} - |{\downarrow\downarrow\uparrow}\rangle_{\mathbb{A}} - \tfrac{g_1}{\tilde{g}}|{\uparrow\downarrow\downarrow}\rangle_{\mathbb{B}} + \tfrac{g_2}{\tilde{g}}|{\downarrow\uparrow\downarrow}\rangle_{\mathbb{B}} + \tfrac{g_1-g_2}{\tilde{g}}|{\downarrow\downarrow\uparrow}\rangle_{\mathbb{B}}\Big), \\
|\psi_4^{(\rm D1)}\rangle &= \tfrac{1}{2}\Big(|{\downarrow\uparrow\downarrow}\rangle_{\mathbb{A}} - |{\downarrow\downarrow\uparrow}\rangle_{\mathbb{A}} - \tfrac{g_2}{\tilde{g}}|{\uparrow\downarrow\downarrow}\rangle_{\mathbb{B}} - \tfrac{g_1-g_2}{\tilde{g}}|{\downarrow\uparrow\downarrow}\rangle_{\mathbb{B}} + \tfrac{g_1}{\tilde{g}}|{\downarrow\downarrow\uparrow}\rangle_{\mathbb{B}}\Big),
\end{aligned} \tag{18}$$

$$E^{(\rm D2)} = -\frac{3}{4}J_{\rm nn} + \sqrt{g_1^2 - g_1g_2 + g_2^2}$$

$$\begin{aligned}
|\psi_1^{(\rm D2)}\rangle &= \tfrac{1}{2}\Big(|{\uparrow\uparrow\downarrow}\rangle_{\mathbb{A}} - |{\downarrow\uparrow\uparrow}\rangle_{\mathbb{A}} + \tfrac{g_1-g_2}{\tilde{g}}|{\uparrow\uparrow\downarrow}\rangle_{\mathbb{B}} + \tfrac{g_2}{\tilde{g}}|{\uparrow\downarrow\uparrow}\rangle_{\mathbb{B}} - \tfrac{g_1}{\tilde{g}}|{\downarrow\uparrow\uparrow}\rangle_{\mathbb{B}}\Big), \\
|\psi_2^{(\rm D2)}\rangle &= \tfrac{1}{2}\Big(|{\uparrow\downarrow\uparrow}\rangle_{\mathbb{A}} - |{\downarrow\uparrow\uparrow}\rangle_{\mathbb{A}} - \tfrac{g_2}{\tilde{g}}|{\uparrow\uparrow\downarrow}\rangle_{\mathbb{B}} + \tfrac{g_1}{\tilde{g}}|{\uparrow\downarrow\uparrow}\rangle_{\mathbb{B}} - \tfrac{g_1-g_2}{\tilde{g}}|{\downarrow\uparrow\uparrow}\rangle_{\mathbb{B}}\Big), \\
|\psi_3^{(\rm D2)}\rangle &= \tfrac{1}{2}\Big(|{\uparrow\downarrow\downarrow}\rangle_{\mathbb{A}} - |{\downarrow\downarrow\uparrow}\rangle_{\mathbb{A}} + \tfrac{g_1}{\tilde{g}}|{\uparrow\downarrow\downarrow}\rangle_{\mathbb{B}} - \tfrac{g_2}{\tilde{g}}|{\downarrow\uparrow\downarrow}\rangle_{\mathbb{B}} - \tfrac{g_1-g_2}{\tilde{g}}|{\downarrow\downarrow\uparrow}\rangle_{\mathbb{B}}\Big), \\
|\psi_4^{(\rm D2)}\rangle &= \tfrac{1}{2}\Big(|{\downarrow\uparrow\downarrow}\rangle_{\mathbb{A}} - |{\downarrow\downarrow\uparrow}\rangle_{\mathbb{A}} + \tfrac{g_2}{\tilde{g}}|{\uparrow\downarrow\downarrow}\rangle_{\mathbb{B}} + \tfrac{g_1-g_2}{\tilde{g}}|{\downarrow\uparrow\downarrow}\rangle_{\mathbb{B}} - \tfrac{g_1}{\tilde{g}}|{\downarrow\downarrow\uparrow}\rangle_{\mathbb{B}}\Big),
\end{aligned} \tag{19}$$

$$E^{(\rm D3)} = \frac{3}{4}J_{\rm nn} + g_1 + g_2$$

$$\begin{aligned}
|\psi_1^{(\rm D3)}\rangle &= \tfrac{1}{\sqrt{2}}\Big(|{\uparrow\uparrow\uparrow}\rangle_{\mathbb{A}} + |{\uparrow\uparrow\uparrow}\rangle_{\mathbb{B}}\Big), \\
|\psi_2^{(\rm D3)}\rangle &= \tfrac{1}{\sqrt{6}}\Big(|{\uparrow\uparrow\downarrow}\rangle_{\mathbb{A}} + |{\uparrow\downarrow\uparrow}\rangle_{\mathbb{A}} + |{\downarrow\uparrow\uparrow}\rangle_{\mathbb{A}} + |{\uparrow\uparrow\downarrow}\rangle_{\mathbb{B}} + |{\uparrow\downarrow\uparrow}\rangle_{\mathbb{B}} + |{\downarrow\uparrow\uparrow}\rangle_{\mathbb{B}}\Big), \\
|\psi_3^{(\rm D3)}\rangle &= \tfrac{1}{\sqrt{6}}\Big(|{\downarrow\downarrow\uparrow}\rangle_{\mathbb{A}} + |{\downarrow\uparrow\downarrow}\rangle_{\mathbb{A}} + |{\uparrow\downarrow\downarrow}\rangle_{\mathbb{A}} + |{\downarrow\downarrow\uparrow}\rangle_{\mathbb{B}} + |{\downarrow\uparrow\downarrow}\rangle_{\mathbb{B}} + |{\uparrow\downarrow\downarrow}\rangle_{\mathbb{B}}\Big), \\
|\psi_4^{(\rm D3)}\rangle &= \tfrac{1}{\sqrt{2}}\Big(|{\downarrow\downarrow\downarrow}\rangle_{\mathbb{A}} + |{\downarrow\downarrow\downarrow}\rangle_{\mathbb{B}}\Big),
\end{aligned} \tag{20}$$

$$E^{(\mathrm{D4})} = \frac{3}{4}J_{\mathrm{nn}} - g_1 - g_2 \qquad \begin{aligned} |\psi_1^{(\mathrm{D4})}\rangle &= \tfrac{1}{\sqrt{2}}\Big(|\uparrow\uparrow\uparrow\rangle_{\mathbb{A}} - |\uparrow\uparrow\uparrow\rangle_{\mathbb{B}}\Big), \\ |\psi_2^{(\mathrm{D4})}\rangle &= \tfrac{1}{\sqrt{6}}\Big(|\uparrow\uparrow\downarrow\rangle_{\mathbb{A}} + |\uparrow\downarrow\uparrow\rangle_{\mathbb{A}} + |\downarrow\uparrow\uparrow\rangle_{\mathbb{A}} - |\uparrow\uparrow\downarrow\rangle_{\mathbb{B}} - |\uparrow\downarrow\uparrow\rangle_{\mathbb{B}} - |\downarrow\uparrow\uparrow\rangle_{\mathbb{B}}\Big), \\ |\psi_3^{(\mathrm{D4})}\rangle &= \tfrac{1}{\sqrt{6}}\Big(|\downarrow\downarrow\uparrow\rangle_{\mathbb{A}} + |\downarrow\uparrow\downarrow\rangle_{\mathbb{A}} + |\uparrow\downarrow\downarrow\rangle_{\mathbb{A}} - |\downarrow\downarrow\uparrow\rangle_{\mathbb{B}} - |\downarrow\uparrow\downarrow\rangle_{\mathbb{B}} - |\uparrow\downarrow\downarrow\rangle_{\mathbb{B}}\Big), \\ |\psi_4^{(\mathrm{D4})}\rangle &= \tfrac{1}{\sqrt{2}}\Big(|\downarrow\downarrow\downarrow\rangle_{\mathbb{A}} - |\downarrow\downarrow\downarrow\rangle_{\mathbb{B}}\Big), \end{aligned} \tag{21}$$

where $\tilde{g} = \sqrt{g_1^2 - g_1 g_2 + g_2^2}$. When $g_1 < 0$ and $g_2 < 0$, $E^{(\mathrm{D3})}$ with a totally symmetric superposition of the $|\mathbb{A}\rangle$ and $|\mathbb{B}\rangle$ plaquettes is the ground state of $\mathcal{H}_{\mathrm{D}}$. On the other hand, the ground state is given by $E^{(\mathrm{D1})}$ either when *i*) $g_1 < 0$ and $g_2 < 0$ and $J_{\mathrm{nn}} > \frac{2}{3}(-g_1 - g_2 - \tilde{g})$, or when *ii*) $g_1$ and $g_2$ have opposite signs regardless of $J_{\mathrm{nn}}$. This state is formed by valence bonds at the resonating hexagons with dangling spins.

Specific heat and spin susceptibility of $\mathcal{H}_{\mathrm{D}}$ calculated on a single hexagon with the model parameters for $LiZn_2Mo_3O_8$ are shown in Supplementary Figure 5.

## SUPPLEMENTARY NOTE 3: CLUSTER HUBBARD MODEL

When $|t| \sim V'$, the perturbation theory with respect to $t/V'$ breaks down. In this case, the original single-orbital Hubbard model from Eq. (1) can be reformulated by grouping the atomic states at the $\mathcal{T}$ triangles:

$$\mathcal{H}_{\rm C} = \mathcal{H}_{\rm CF} + \mathcal{H}_{\rm kin} + \mathcal{H}_{\mathcal{U}} + \mathcal{H}_{\mathcal{V}} + \mathcal{H}_{\mathcal{V}'}, \tag{22}$$

where the "crystal-field" and intercluster hopping terms are given as:

$$\mathcal{H}_{\rm CF} = \frac{\Delta}{3} \sum_{\substack{i,mm' \in \mathcal{T} \\ \sigma}} c^{\dagger\sigma}_{im} \begin{pmatrix} 0 & 1 & 1 \\ 1 & 0 & 1 \\ 1 & 1 & 0 \end{pmatrix}_{mm'} c^{\sigma}_{im'} \qquad \mathcal{H}_{\rm kin} = \sum_{\substack{\langle ij \rangle, mm' \in \mathcal{T}' \\ \sigma}} t' c^{\dagger\sigma}_{im} c^{\sigma}_{jm'}, \tag{23}$$

respectively, with $\Delta = 3t$; the intracluster Coulomb interactions are:

$$\mathcal{H}_{\mathcal{U}} = \sum_{i,mm' \in \mathcal{T}} \mathcal{U}_{mm'} n^{\uparrow}_{im} n^{\downarrow}_{im'} \qquad \mathcal{H}_{\mathcal{V}} = \sum_{\substack{i,\langle mm' \rangle \in \mathcal{T} \\ \sigma}} \mathcal{V}_{mm'} n^{\sigma}_{im} n^{\sigma}_{im'} \tag{24}$$

with

$$\mathcal{U} = \begin{pmatrix} U & V & V \\ V & U & V \\ V & V & U \end{pmatrix} \qquad \mathcal{V} = V \begin{pmatrix} 0 & 1 & 1 \\ 1 & 0 & 1 \\ 1 & 1 & 0 \end{pmatrix}, \tag{25}$$

and the intercluster Coulomb interactions are (neglecting $J' \sim 0$ and $J' \sim 0$):

$$\mathcal{H}_{\mathcal{V}'} = \sum_{\langle ij \rangle, mm' \in \mathcal{T}'} \mathcal{V}'_{mm'} n^{\uparrow}_{im} n^{\downarrow}_{jm'} + \sum_{\substack{\langle ij \rangle, \langle mm' \rangle \in \mathcal{T}' \\ \sigma}} \mathcal{V}'_{mm'} n^{\sigma}_{im} n^{\sigma}_{jm'} \tag{26}$$

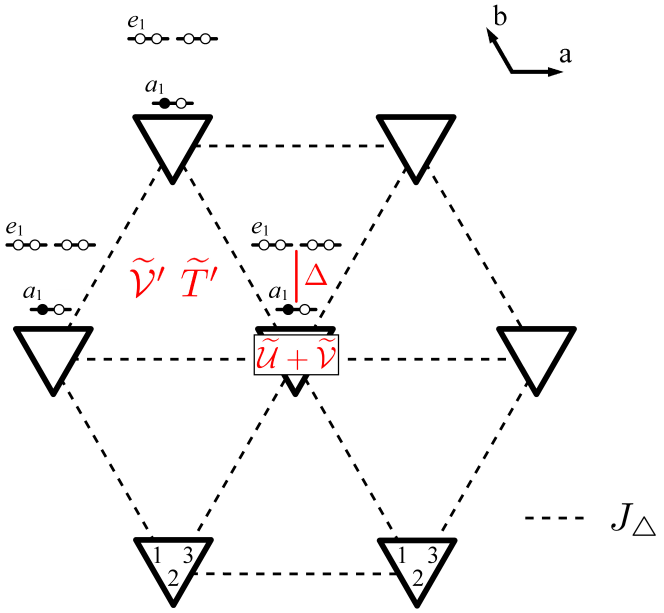


**Supplementary Figure 6**. Schematics of the extended Hubbard model on the triangular lattice formed by the $\mathcal{T}$ clusters, where $\widetilde{\mathcal{U}} + \widetilde{\mathcal{V}}$ and $\widetilde{\mathcal{V}}'$ stand for the intracluster and intercluster Coulomb interactions, respectively, and $\widetilde{T}'$ is the intercluster hopping parameter. The indices 1, 2, 3 number atomic positions at each $\mathcal{T}$ cluster.

with

$$\mathcal{V}' = V' \begin{pmatrix} 0 & 1 & 1 \\ 1 & 0 & 1 \\ 1 & 1 & 0 \end{pmatrix}. \tag{27}$$

Here, $i$ and $j$ run over all $\mathcal{T}$ clusters, and $m$ and $m'$ are the intracluster indices taken as ordered in Supplementary Figure 6. The term $\mathcal{H}_{\rm CF}$ has the form of trigonal distortion along the local $C_3$ axis, $\mathbf{n} = -(\frac{1}{\sqrt{3}}, \frac{1}{\sqrt{3}}, \frac{1}{\sqrt{3}})$. The corresponding rotation $R$ to the local trigonal frame $(x', y', z')$ with $z' \parallel \mathbf{n}$ transforms the electronic states into the single $a_1$ and double-degenerate $e_1$ states with energy levels $\frac{2\Delta}{3}$ and $-\frac{\Delta}{3}$, respectively, as $|\tilde{i}\rangle = \mathcal{D}(R)|i\rangle$, where $|i\rangle \in \{|1\rangle, |2\rangle, |3\rangle\}$, $|\tilde{i}\rangle \in \{|a_1\rangle, |e_1\rangle^{(1)}, |e_1^{(2)}\rangle\}$, and:

$$\mathcal{D}(R) = R = \begin{pmatrix} \frac{1}{\sqrt{3}} & \frac{1}{\sqrt{2}} & -\frac{1}{\sqrt{6}} \\ \frac{1}{\sqrt{3}} & -\frac{1}{\sqrt{2}} & -\frac{1}{\sqrt{6}} \\ \frac{1}{\sqrt{3}} & 0 & \frac{2}{\sqrt{6}} \end{pmatrix}. \tag{28}$$

These states can be further taken as a liner combination (in analogy with the $t_{2g}$ electrons so as to diagonalise the orbital angular momentum operator in the local frame, $L_{z'} = \mathcal{D}(R) L_z \mathcal{D}^{-1}(R)$):

$$\begin{aligned} |a\rangle &= \frac{1}{\sqrt{3}}\big(|1\rangle + |2\rangle + |3\rangle\big), \\ |e_1^{(1)}\rangle &= \frac{1}{\sqrt{3}}\big(w|1\rangle + \bar{w}|2\rangle + |3\rangle\big), \\ |e_1^{(2)}\rangle &= \frac{1}{\sqrt{3}}\big(\bar{w}|1\rangle + w|2\rangle + |3\rangle\big), \end{aligned} \tag{29}$$

where $w = e^{2\pi \mathrm{i}/3}$. Using the inverse transformation $|i\rangle = \Omega|\tilde{i}\rangle$:

$$\Omega = \frac{1}{\sqrt{3}} \begin{pmatrix} 1 & \bar{w} & w \\ 1 & w & \bar{w} \\ 1 & 1 & 1 \end{pmatrix}, \tag{30}$$

the Hamiltonian in Eq. (22) can be rewritten in the "molecular" basis $|\tilde{i}\rangle$, where the interaction terms are:

$$\widetilde{\mathcal{U}} = \frac{U+2V}{3} \begin{pmatrix} 1 & 1 & 1 \\ 1 & 1 & 1 \\ 1 & 1 & 1 \end{pmatrix} \qquad \widetilde{\mathcal{V}} = \frac{2V}{3} \begin{pmatrix} 1 & 1 & 1 \\ 1 & 1 & 1 \\ 1 & 1 & 1 \end{pmatrix} \qquad \widetilde{\mathcal{V}}' = \frac{2V'}{3} \begin{pmatrix} 1 & 1 & 1 \\ 1 & 1 & 1 \\ 1 & 1 & 1 \end{pmatrix}, \tag{31}$$

and the intercluster hopping parameters are $\widetilde{T}' = \Omega^\dagger T' \Omega$. Importantly, when $\Delta < 0$ ($t < 0$) the electrons occupy the $a_1$ state at the $\mathcal{T}$ clusters. Thus, the original single-orbital electronic model on the kagomé lattice is now mapped onto the three-orbital cluster Hubbard model on the triangular lattice, as schematically shown in Supplementary Figure 6. In the limit $t' \ll U$, the theory of superexchange can be applied by considering electron hoppings between two neighbouring clusters, for example:

$$T'_{100} = \begin{pmatrix} 0 & 0 & 0 \\ 0 & 0 & 0 \\ t' & 0 & 0 \end{pmatrix} \longrightarrow \widetilde{T}'_{100} = \frac{t'}{3} \begin{pmatrix} 1 & \bar{w} & w \\ 1 & \bar{w} & w \\ 1 & \bar{w} & w \end{pmatrix} \qquad T'_{-100} = \begin{pmatrix} 0 & 0 & t' \\ 0 & 0 & 0 \\ 0 & 0 & 0 \end{pmatrix} \longrightarrow \widetilde{T}'_{-100} = \frac{t'}{3} \begin{pmatrix} 1 & 1 & 1 \\ w & w & w \\ \bar{w} & \bar{w} & \bar{w} \end{pmatrix}. \tag{32}$$

Then, the corresponding spin Hamiltonian is derived to second order in $t'/U$ and $t'/\Delta$:

$$\mathcal{H}_\triangle = \sum_{\langle ij \rangle} J_\triangle \mathbf{S}_i \cdot \mathbf{S}_j \tag{33}$$

with

$$J_\triangle = -\frac{8t'^2}{3(2V + 3|\Delta| - 2V')} + \frac{4t'^2}{3(U + 2V - 2V')} + \frac{8t'^2}{3(U + 2V + 3|\Delta| - 2V')}. \tag{34}$$

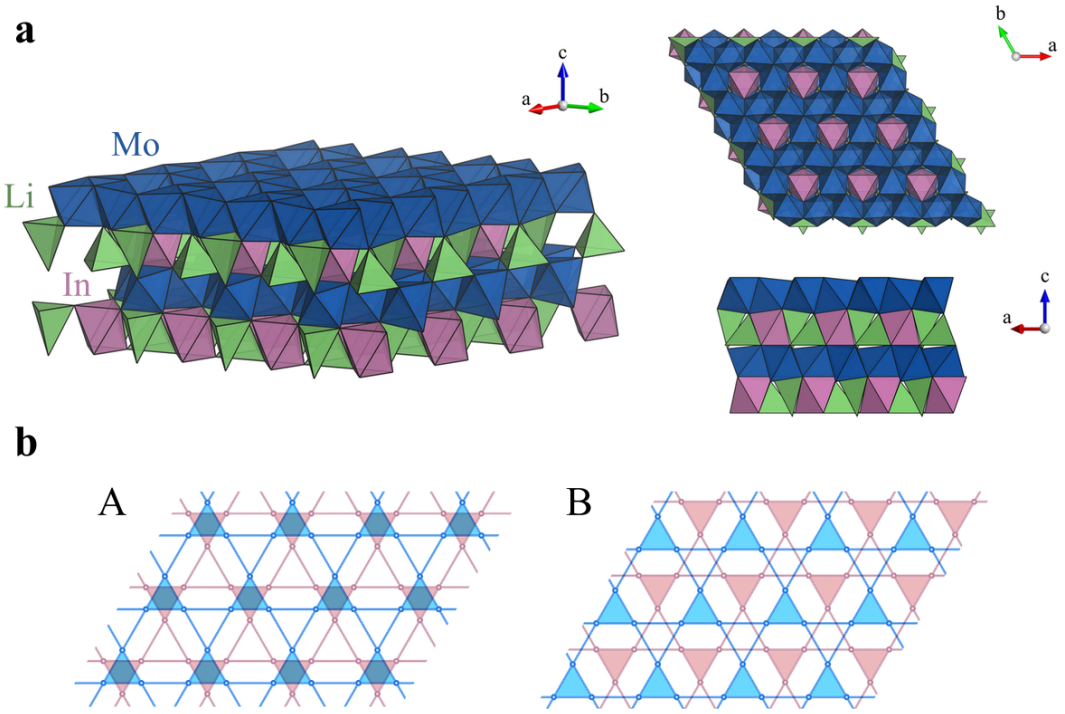


**Supplementary Figure 7**. **a** Crystal structure of $Li_2InMo_3O_8$. **b** Two stacking types of the kagomé lattices along the $c$ axis (blue and pink colours correspond to different layers). $Li_2InMo_3O_8$ and $Li_2ScMo_3O_8$ correspond to the BB stacking, and $LiZn_2Mo_3O_8$ corresponds to the ABABAB stacking.

## SUPPLEMENTARY NOTE 4: FIRST-PRINCIPLES CALCULATIONS

The crystal structure of $Li_2InMo_3O_8$ is shown in Supplementary Figure 7, and the corresponding crystallographic parameters of $Li_2InMo_3O_8$ and $Li_2ScMo_3O_8$ are given in Supplementary Table 1. The crystal structure parameters of $LiZn_2Mo_3O_8$ are presented in Supplementary Table 2.

The band structures of $Li_2InMo_3O_8$ and $Li_2ScMo_3O_8$ with spin-orbit coupling are shown in Supplementary Figure 8. The effect of spin-orbit coupling gives a small band splitting of the $a_1$ and $e_1$ states and can be discarded from the model construction. However, it is worth noting that spin-orbit coupling is important to reproduce spin wave excitations in $Li_2InMo_3O_8$ and $Li_2ScMo_3O_8$ that were reported to have a spin gap due to anisotropic magnetic interactions [5].

The resulting Wannier functions representing the $a_1$ and $e_1$ states for $Li_2InMo_3O_8$ are shown in Supplementary Figure 9. The calculated spreads of the Wannier functions are 3.92 Å$^2$, 3.70 Å$^2$, and 3.36 Å$^2$ for $Li_2InMo_3O_8$, $Li_2ScMo_3O_8$, and $LiZn_2Mo_3O_8$, respectively. The full list of hopping parameters for $Li_2InMo_3O_8$ and $Li_2ScMo_3O_8$ is given in Supplementary Tables 3 and 4, respectively. Hopping parameters for $Li_2InMo_3O_8$ are presented in Supplementary Table 5. The parameters of Coulomb and exchange interactions were calculated within random-phase approximation in the basis of Wannier functions [8, 9]. The values of $J$ and $J'$ were found to be less that 0.01 eV and can be neglected from the consideration.

Finally, the $Mo_3O_{13}$ layers possess different types of stacking, as shown in Supplementary Figure 7. The interlayer hopping parameters of the B type in each system are small and can be neglected. The interlayer hopping parameters of the A type in $LiZn_2Mo_3O_8$ can lead to the interlayer exchange comparable to $J_{\rm nn}$ between intralayer next-nearest neighbours and are expected to give a small change to the final $T_C$ without destroying the plaquette charge order.

**Supplementary Table 1**. Crystal structure and Wyckoff positions of $Li_2InMo_3O_8$ and $Li_2ScMo_3O_8$ as determined from powder x-ray diffraction [10]. The space group is $P6_3mc$.

| Atom | Wyck. Pos. | x | y | z |
|---|---|---|---|---|
| $Li_2InMo_3O_8$ ($a = 5.7846$ Å $c = 10.4475$ Å) | | | | |
| Li | $2a$ | 0 | 0 | 0.1678 |
| Li | $2b$ | 1/3 | 2/3 | 0.0825 |
| In | $2b$ | 1/3 | 2/3 | 0.6744 |
| Mo | $6c$ | 0.1876 | 0.8124 | 0.3931 |
| O | $6c$ | 0.5190 | 0.4810 | 0.0261 |
| O | $6c$ | 0.8421 | 0.1579 | 0.2940 |
| O | $2a$ | 0 | 0 | 0 |
| O | $2b$ | 1/3 | 2/3 | 0.2579 |
| $Li_2ScMo_3O_8$ ($a = 5.7732$ Å $c = 10.2880$ Å) | | | | |
| Li | $2a$ | 0 | 0 | 0.1689 |
| Li | $2b$ | 1/3 | 2/3 | 0.0836 |
| Sc | $2b$ | 1/3 | 2/3 | 0.6732 |
| Mo | $6c$ | 0.1870 | 0.8130 | 0.3916 |
| O | $6c$ | 0.5193 | 0.4807 | 0.0319 |
| O | $6c$ | 0.8429 | 0.1571 | 0.2862 |
| O | $2a$ | 0 | 0 | 0 |
| O | $2b$ | 1/3 | 2/3 | 0.2585 |

**Supplementary Table 2**. Crystal structure and Wyckoff positions of $LiZn_2Mo_3O_8$ as determined from neutron powder diffraction [11]. The space group is $R\bar{3}m$.

| Atom | Wyck. Pos. | x | y | z | occ. |
|---|---|---|---|---|---|
| $LiZn_2Mo_3O_8$ ($a = 5.7956$ Å $c = 31.039$ Å) | | | | | |
| Mo | $18h$ | 0.18493 | 0.81507 | 0.08372 | 1.0 |
| O | $18h$ | 0.84510 | 0.15490 | 0.04788 | 1.0 |
| O | $18h$ | 0.49240 | 0.50760 | 0.12458 | 1.0 |
| O | $6c$ | 0 | 0 | 0.11841 | 1.0 |
| O | $6c$ | 0 | 0 | 0.37140 | 1.0 |
| Zn | $6c$ | 1/3 | 2/3 | -0.64229 | 1.0 |
| Zn | $6c$ | 0 | 0 | 0.18144 | 1.0 |
| Li | $6c$ | 0 | 0 | 0.50510 | 0.5 |
| Li | $3a$ | 0 | 0 | 0 | 1.0 |

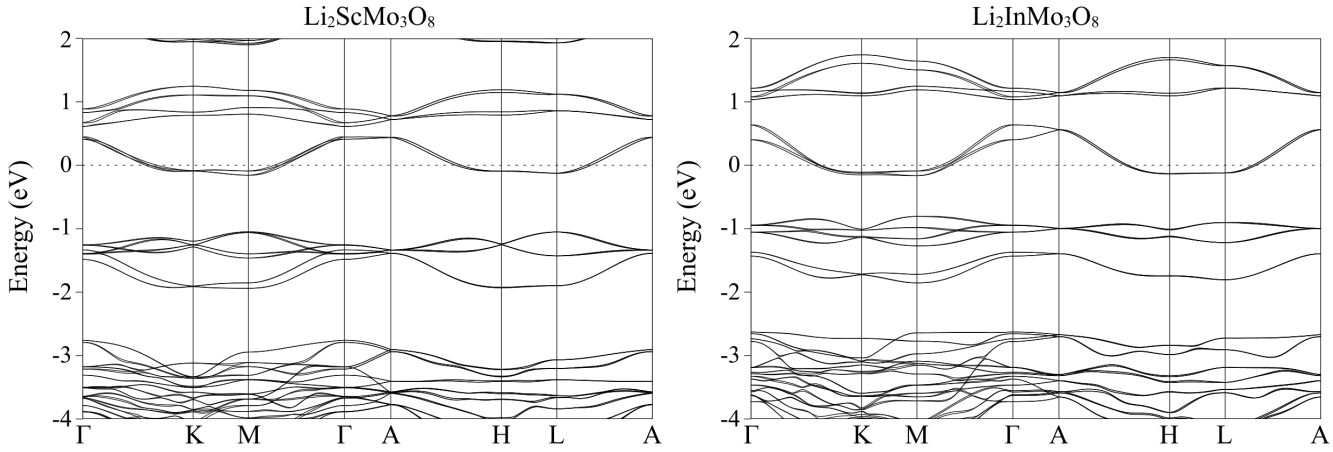


**Supplementary Figure 8**. Band structures of $Li_2ScMo_3O_8$ and $Li_2InMo_3O_8$ from local density approximation with spin-orbit coupling.

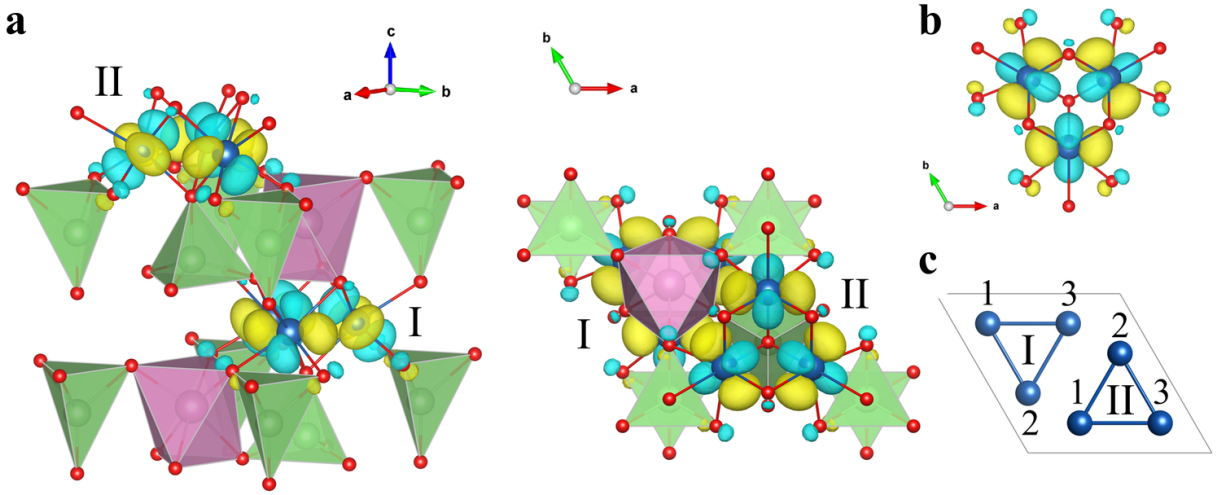


**Supplementary Figure 9**. **a** Wannier functions representing the $a_1$ and $e_1$ states in $Li_2InMo_3O_8$ as obtained from LDA calculations; I and II denote two clusters in the unit cell. **b** Wannier functions in the $Mo_3O_{13}$ cluster. **c** Order of the Wanner functions for two $Mo_3O_{13}$ clusters in the unit cell of $Li_2InMo_3O_8$.

**Supplementary Table 3**. Hopping parameters (in meV) for the one-orbital model in $Li_2InMo_3O_8$ as obtained from LDA calculations. The unit cell contains two $Mo_3O_{13}$ clusters I and II centered at $(\frac{1}{3}, \frac{2}{3}, 0.3931)$ and $(\frac{2}{3}, \frac{1}{3}, 0.8931)$ in fractional units, respectively. Atomic coordinates of the Mo sites in each clusters are given in fractional units as $(0.1876, 0.8124, 0.3931)$, $(0.1876, 0.3752, 0.3931)$, $(0.6248, 0.8124, 0.3931)$ for cluster I, and $(0.8124, 0.1876, 0.8931)$, $(0.8124, 0.6248, 0.8931)$, $(0.3752, 0.1876, 0.8931)$ for cluster II, and their order is shown in Supplementary Figure 9c. The lattice translations are $a(1,0,0)$, $a(-\frac{1}{2}, \frac{\sqrt{3}}{2}, 0)$, $(0,0,c)$, with $a = 5.7846$ Å and $c = 10.4475$ Å.

Intracluster hoppings

$$\hat{t}^{\mathrm{I,I}}_{[000]} = \hat{t}^{\mathrm{II,II}}_{[000]} = \begin{pmatrix} 0 & -409.1 & -409.1 \\ -409.1 & 0 & -409.1 \\ -409.1 & -409.1 & 0 \end{pmatrix}$$

Intercluster hoppings

Intralayer nearest neighbours $\left(\hat{t}^{\mathrm{II,II}}_{ij} = [\hat{t}^{\mathrm{I,I}}_{ij}]^T\right)$

$$\hat{t}^{\mathrm{I,I}}_{[100]} = \begin{pmatrix} 15.8 & 10.0 & -0.8 \\ 8.1 & -15.8 & 10.0 \\ 181.2 & 8.1 & 15.8 \end{pmatrix} \quad \hat{t}^{\mathrm{I,I}}_{[\bar{1}00]} = \begin{pmatrix} 15.8 & 8.1 & 181.2 \\ 10.0 & -15.8 & 8.1 \\ -0.8 & 10.0 & 15.8 \end{pmatrix} \quad \hat{t}^{\mathrm{I,I}}_{[110]} = \begin{pmatrix} -15.8 & 8.1 & 10.0 \\ 10.0 & 15.8 & -0.8 \\ 8.1 & 181.2 & 15.8 \end{pmatrix}$$

$$\hat{t}^{\mathrm{I,I}}_{[010]} = \begin{pmatrix} 15.8 & 181.2 & 8.1 \\ -0.8 & 15.8 & 10.0 \\ 10.0 & 8.1 & -15.8 \end{pmatrix} \quad \hat{t}^{\mathrm{I,I}}_{[0\bar{1}0]} = \begin{pmatrix} 15.8 & -0.8 & 10.0 \\ 181.2 & 15.8 & 8.1 \\ 8.1 & 10.0 & -15.8 \end{pmatrix} \quad \hat{t}^{\mathrm{I,I}}_{[\bar{1}\bar{1}0]} = \begin{pmatrix} -15.8 & 10.0 & 8.1 \\ 8.1 & 15.8 & 181.2 \\ 10.0 & -0.8 & 15.8 \end{pmatrix}$$

Interlayer nearest neighbours $\left(\hat{t}^{\mathrm{II,I}}_{ij} = \hat{t}^{\mathrm{I,II}}_{ij}\right)$

$$\hat{t}^{\mathrm{I,II}}_{[000]} = \begin{pmatrix} -11.6 & -1.6 & -1.6 \\ -12.0 & -7.5 & 12.0 \\ -12.0 & 12.0 & -7.5 \end{pmatrix} \quad \hat{t}^{\mathrm{I,II}}_{[\bar{1}00]} = \begin{pmatrix} -7.5 & 12.0 & -12.0 \\ 12.0 & -7.5 & -12.0 \\ -1.6 & -1.6 & -11.6 \end{pmatrix} \quad \hat{t}^{\mathrm{I,II}}_{[010]} = \begin{pmatrix} -7.5 & -12.0 & 12.0 \\ -1.6 & -11.6 & -1.6 \\ 12.0 & -12.0 & -7.5 \end{pmatrix}$$

$$\hat{t}^{\mathrm{I,II}}_{[\bar{1}0\bar{1}]} = \begin{pmatrix} -7.5 & 12.0 & -1.6 \\ 12.0 & -7.5 & -1.6 \\ -12.0 & -12.0 & -11.6 \end{pmatrix} \quad \hat{t}^{\mathrm{I,II}}_{[00\bar{1}]} = \begin{pmatrix} -11.6 & -12.0 & -12.0 \\ -1.6 & -7.5 & 12.0 \\ -1.6 & 12.0 & -7.5 \end{pmatrix} \quad \hat{t}^{\mathrm{I,II}}_{[01\bar{1}]} = \begin{pmatrix} -7.5 & -1.6 & 12.0 \\ -12.0 & -11.6 & -12.0 \\ 12.0 & -1.6 & -7.5 \end{pmatrix}$$

**Supplementary Table 4**. Hopping parameters (in meV) for the one-orbital model in $Li_2ScMo_3O_8$ as obtained from LDA calculations. The unit cell contains two $Mo_3O_{13}$ clusters I and II centered at $(\frac{1}{3}, \frac{2}{3}, 0.3916)$ and $(\frac{2}{3}, \frac{1}{3}, 0.8916)$ in fractional units, respectively. Atomic coordinates of the Mo sites in each clusters are given in fractional units as $(0.187, 0.813, 0.3916)$, $(0.187, 0.374, 0.3916)$, $(0.626, 0.813, 0.3916)$ for cluster I, and $(0.813, 0.187, 0.8916)$, $(0.813, 0.626, 0.8916)$, $(0.374, 0.187, 0.8916)$ for cluster II, and their order is shown in Supplementary Figure 9c. The lattice translations are $a(1, 0, 0)$, $a(-\frac{1}{2}, \frac{\sqrt{3}}{2}, 0)$, $(0, 0, c)$, with $a = 5.7732$ Å and $c = 10.2880$ Å.

Intracluster hoppings

$$\hat{t}^{\mathrm{I,I}}_{[000]} = \hat{t}^{\mathrm{II,II}}_{[000]} = \begin{pmatrix} 0 & -281.2 & -281.2 \\ -281.2 & 0 & -281.2 \\ -281.2 & -281.2 & 0 \end{pmatrix}$$

Intercluster hoppings

Intralayer nearest neighbours $\left(\hat{t}^{\mathrm{II,II}}_{ij} = [\hat{t}^{\mathrm{I,I}}_{ij}]^T\right)$

$$\hat{t}^{\mathrm{I,I}}_{[100]} = \begin{pmatrix} 16.6 & 1.4 & 2.8 \\ 13.8 & -24.7 & 1.4 \\ 146.7 & 13.7 & 16.6 \end{pmatrix} \quad \hat{t}^{\mathrm{I,I}}_{[\bar{1}00]} = \begin{pmatrix} 16.6 & 13.8 & 146.7 \\ 1.4 & -24.7 & 13.8 \\ 2.8 & 1.4 & 16.6 \end{pmatrix} \quad \hat{t}^{\mathrm{I,I}}_{[110]} = \begin{pmatrix} -24.7 & 13.8 & 1.4 \\ 1.4 & 16.6 & 2.8 \\ 13.8 & 146.7 & 16.6 \end{pmatrix}$$

$$\hat{t}^{\mathrm{I,I}}_{[010]} = \begin{pmatrix} 16.6 & 146.7 & 13.8 \\ 2.8 & 16.6 & 1.4 \\ 1.4 & 13.8 & -24.7 \end{pmatrix} \quad \hat{t}^{\mathrm{I,I}}_{[0\bar{1}0]} = \begin{pmatrix} 16.6 & 2.8 & 1.4 \\ 146.7 & 16.6 & 13.8 \\ 13.8 & 1.4 & -24.7 \end{pmatrix} \quad \hat{t}^{\mathrm{I,I}}_{[\bar{1}\bar{1}0]} = \begin{pmatrix} -24.7 & 1.4 & 13.8 \\ 13.8 & 16.6 & 146.7 \\ 1.4 & 2.8 & 16.6 \end{pmatrix}$$

Interlayer nearest neighbours $\left(\hat{t}^{\mathrm{II,I}}_{ij} = \hat{t}^{\mathrm{I,II}}_{ij}\right)$

$$\hat{t}^{\mathrm{I,II}}_{[000]} = \begin{pmatrix} -7.4 & 5.3 & 5.3 \\ -3.1 & 20.3 & -8.5 \\ -3.1 & -8.5 & 20.3 \end{pmatrix} \quad \hat{t}^{\mathrm{I,II}}_{[\bar{1}00]} = \begin{pmatrix} 20.3 & -8.5 & -3.1 \\ -8.5 & 20.3 & -3.1 \\ 5.3 & 5.3 & -7.4 \end{pmatrix} \quad \hat{t}^{\mathrm{I,II}}_{[010]} = \begin{pmatrix} 20.3 & -3.1 & -8.5 \\ 5.3 & -7.4 & 5.3 \\ -8.5 & -3.1 & 20.3 \end{pmatrix}$$

$$\hat{t}^{\mathrm{I,II}}_{[\bar{1}0\bar{1}]} = \begin{pmatrix} 20.3 & -8.5 & 5.3 \\ -8.5 & 20.3 & 5.3 \\ -3.1 & -3.1 & -7.4 \end{pmatrix} \quad \hat{t}^{\mathrm{I,II}}_{[00\bar{1}]} = \begin{pmatrix} -7.4 & -3.1 & -3.1 \\ 5.3 & 20.3 & -8.5 \\ 5.3 & -8.5 & 20.3 \end{pmatrix} \quad \hat{t}^{\mathrm{I,II}}_{[01\bar{1}]} = \begin{pmatrix} 20.3 & 5.3 & -8.5 \\ -3.1 & -7.4 & -3.1 \\ -8.5 & 5.3 & 20.3 \end{pmatrix}$$

**Supplementary Table 5**. Hopping parameters (in meV) for the one-orbital model in $LiZn_2Mo_3O_8$ as obtained from LDA calculations. The unit cell contains six $Mo_3O_{13}$ clusters, centered at $(\frac{1}{3}, \frac{2}{3}, 0.083720)$, $(\frac{1}{3}, \frac{2}{3}, 0.249613)$, $(0, 0, 0.417053)$, $(0, 0, 0.582947)$, $(\frac{2}{3}, \frac{1}{3}, 0.750387)$, and $(\frac{2}{3}, \frac{1}{3}, 0.916280)$. Here, the hopping parameters are shown for cluster I. Atomic coordinates of the Mo sites in the clusters are given in fractional units as $(0.18493, 0.81507, 0.08372)$, $(0.18493, 0.36986, 0.08372)$, and $(0.63014, 0.81507, 0.08372)$ for cluster I, $(0.481737, 0.518263, 0.249613)$, $(0.481737, 0.963473, 0.249613)$, and $(0.036527, 0.518263, 0.249613)$ for cluster II, $(0.81507, 0.18493, 0.91628)$, $(0.81507, 0.63014, 0.91628)$, and $(0.36986, 0.18493, 0.91628)$ for cluster VI. The lattice translations are $a(1, 0, 0)$, $a(-\frac{1}{2}, \frac{\sqrt{3}}{2}, 0)$, $(0, 0, c)$, with $a = 5.7956$ Å and $c = 31.039$ Å.

Intracluster hoppings

$$\hat{t}^{\mathrm{I,I}}_{[000]} = \begin{pmatrix} 0 & -134.3 & -134.3 \\ -134.3 & 0 & -134.3 \\ -134.3 & -134.3.2 & 0 \end{pmatrix}$$

Intercluster hoppings

Intralayer nearest neighbours

$$\hat{t}^{\mathrm{I,I}}_{[0\bar{1}0]} = \begin{pmatrix} 27.9 & -7.8 & 7.3 \\ 113.3 & 27.9 & -25.6 \\ -25.6 & 7.3 & -58.0 \end{pmatrix} \quad \hat{t}^{\mathrm{I,I}}_{[010]} = \begin{pmatrix} 27.9 & 113.3 & -25.6 \\ -7.8 & 27.9 & 7.3 \\ 7.3 & -25.6 & -58.0 \end{pmatrix} \quad \hat{t}^{\mathrm{I,I}}_{[110]} = \begin{pmatrix} -58.0 & -25.6 & 7.3 \\ 7.3 & 27.9 & -7.8 \\ -25.6 & 113.3 & 27.9 \end{pmatrix}$$

$$\hat{t}^{\mathrm{I,I}}_{[\bar{1}\bar{1}0]} = \begin{pmatrix} -58.0 & 7.3 & -25.6 \\ -25.6 & 27.9 & 113.3 \\ 7.3 & -7.8 & 27.9 \end{pmatrix} \quad \hat{t}^{\mathrm{I,I}}_{[100]} = \begin{pmatrix} 27.9 & 7.3 & -7.8 \\ -25.6 & -58.0 & 7.3 \\ 113.3 & -25.6 & 27.9 \end{pmatrix} \quad \hat{t}^{\mathrm{I,I}}_{[\bar{1}00]} = \begin{pmatrix} 27.9 & -25.6 & 113.3 \\ 7.3 & -58.0 & -25.6 \\ -7.8 & 7.3 & 27.9 \end{pmatrix}$$

Interlayer nearest neighbours

A type

$$\hat{t}^{\mathrm{I,II}}_{[000]} = \begin{pmatrix} -33.1 & -38.8 & -38.8 \\ -38.8 & -33.1 & -38.8 \\ -38.8 & -38.8 & -33.1 \end{pmatrix}$$

B type

$$\hat{t}^{\mathrm{I,VI}}_{[00\bar{1}]} = \begin{pmatrix} -1.2 & 0.5 & 0.5 \\ 0.3 & 0.5 & -6.8 \\ 0.3 & -6.8 & 0.5 \end{pmatrix} \quad \hat{t}^{\mathrm{I,VI}}_{[01\bar{1}]} = \begin{pmatrix} 0.5 & 0.3 & -6.8 \\ 0.5 & -1.2 & 0.5 \\ -6.8 & 0.3 & 0.5 \end{pmatrix} \quad \hat{t}^{\mathrm{I,VI}}_{[\bar{1}0\bar{1}]} = \begin{pmatrix} 0.5 & -6.8 & 0.3 \\ -6.8 & 0.5 & 0.3 \\ 0.5 & 0.5 & -1.2 \end{pmatrix}$$

* nikolaev.s.aa@m.titech.ac.jp

[1] Moessner, R., Sondhi, S. L., Chandra, P. Phase diagram of the hexagonal lattice quantum dimer model. *Phys. Rev. B* **64**, 144416 (2001).
[2] Schlittler, T. M., Mosseri, R., Barthel, T. Phase diagram of the hexagonal lattice quantum dimer model: Order parameters, ground-state energy, and gaps. *Phys. Rev. B* **96** 195142 (2017).
[3] Pollmann, F., Fulde, P., Shtengel, K. Kinetic ferromagnetism on a kagome lattice. *Phys. Rev. Lett.* **100**, 136404 (2008).
[4] Pollmann, F., Roychowdhury, K., Hotta, C., Penc, K. Interplay of charge and spin fluctuations of strongly interacting electrons on the kagome lattice. *Phys. Rev. B* **90**, 035118 (2014).
[5] Iida, K. et al. Quantum magnetisms in uniform triangular lattices $Li_2AMo_3O_8$ (A=In, Sc). *Sci. Rep.* **9**, 1826 (2019).
[6] Marzari, N. et al. Maximally localized Wannier functions: Theory and applications. *Rev. Mod. Phys.* **84**, 1419–1475 (2012).
[7] Mostofi, A. A. et al. An updated version of wannier90: A tool for obtaining maximally-localised Wannier functions. *Comput. Phys. Commun.* **185**, 2309–2310 (2014).
[8] Springer, M. & Aryasetiawan, F. Frequency-dependent screened interaction in Ni within the random-phase approximation. *Phys. Rev. B* **57**, 4364–4368 (1998).
[9] Aryasetiawan, F., Imada, M., Georges, A., Kotliar, G., Biermann, S., Lichtenstein, A. I. Frequency-dependent local interactions and low-energy effective models from electronic structure calculations. *Phys. Rev. B* **70**, 195104 (2004).
[10] Haraguchi, Yu. et al. Spin-liquid behavior in the spin-frustrated $Mo_3$ cluster magnet $Li_2ScMo_3O_8$ in contrast to magnetic ordering in isomorphic $Li_2InMo_3O_8$. *Phys. Rev. B* **92**, 014409 (2015).
[11] Sandvik, K. E. et al. Controlling the stoichiometry of the triangular lattice antiferromagnet $Li_{1+x}Zn_{2-y}Mo_3O_8$. *Journal of Solid State Chemistry* **271**, 216–221 (2019).